Submitted version of the paper published in J. Power Sources:

https://doi.org/10.1016/j.jpowsour.2022.231638

Exploring Critical Parameters of Electrode Fabrication in Polymer Electrolyte Membrane Fuel Cells

Krishan Talukdar[a], Tobias Morawietz[a,b], Patrick Sarkezi-Selsky[a], Khrystyna Yezerska[c], Oleg Sergeev[c], Jan-Frederik Heger[b], Thomas Jahnke[a], Pawel Gazdzicki[a*] and K. Andreas Friedrich [a,d]

[a]German Aerospace Center (DLR), Institute of Engineering Thermodynamics, Pfaffenwaldring 38-40, 70569 Stuttgart, Germany

[b]Esslingen University of Applied Sciences, Faculty of Science, Energy and Building Services, Kanalstrasse 33, Esslingen 73728, Germany

[c]German Aerospace Center (DLR), Institute of Networked Energy System, Carl-von-Ossietzky-Str. 15, 26129 Oldenburg

[d]University of Stuttgart, Institute of Building Energetics, Thermal Engineering and Energy Storage (IGTE), Pfaffenwaldring 31, 70569 Stuttgart, Germany

Microstructure and electrochemical properties of the cathode catalyst layers (CCL) of a polymer electrolyte membrane fuel cells (PEMFC) have great impact on the performance and durability of the cell. The aim of this work is to make a link between CCL structure and fuel cell

performance. To obtain CCLs with unique structures six types electrodes were prepared each with a different coating technique but with the same Pt loading. The coating techniques are air-brush, screen-printing, inkjet printing, dry-spray, doctor-blade and drop casting. Moreover, intrinsic properties of PEMFC electrodes such as porosity, permeability, diffusivity as well as ionomer distribution are determined by Focused Ion Beam Scanning Electron Microscopy (FIB-SEM) and Atomic Force Microscopy (AFM). Overall, 12 parameters have been evaluated. Generally, CCLs with low fractions of uncovered Pt/C show higher performance at low current densities. In this case the more homogeneous ionomer distribution leads to a higher catalyst utilization. At high current densities transport properties of the CCL have to be considered in addition to the catalyst utilization to explain their performance. The CCL prepared by screen printing shows a low fraction of uncovered Pt/C in combination with good transport properties, leading to the best performance at high currents.

Corresponding author: e-mail: pawel.gazdzicki@dlr.de; Phone: +49-711-6862-8094

Keywords: PEMFC, MEA preparation, catalyst coating, microstructure of catalyst layer, electrode design

1. Introduction

In the quest to reduce greenhouse gas emissions (GHG), “green” hydrogen (generated using electricity from renewable energies) represents a promising energy carrier with a particularly low CO_2 foot print. Polymer electrolyte membrane fuel cells (PEMFC) using green hydrogen as fuel are considered an important technology to reduce GHG emissions [1-3]. PEMFCs have higher storage capacity as well as higher power-to-weight-ratio compared to batteries and are emission-free in contrast to internal combustion engines [4, 5]. However, the biggest obstacle of this technology is the high cost caused mainly by low production volume and the usage of

expensive resources [6-8]. Moreover, mass transport limitations occurring at high current density and at low Pt loadings as well as degradation of the electrodes are still major obstacles in terms of performance and longevity [9-11]. Hence optimizing electrodes remains a great challenge and requires better understanding of the relation between the electrode properties and the electrochemical behavior.

To design an efficient, stable and low platinum loaded electrode it is required to have an active catalyst with high stability and large surface area. In addition, ionomer in contact with the catalyst is necessary to enable ionic conductivity, improve stability and increased reaction inter-phase [12-14]. Forming a porous catalyst layer occurs via a coating process of the catalyst on the substrate (either on the membrane or on the gas diffusion layer). This CL coating process is a critical step in the production of the membrane electrode assembly (MEA) as it determines the properties of the CL to a large extent [15]. In this context catalyst layers should have optimized porosity (35-50 %) and thickness (4-10 µm) with appropriate water management capacity [16-24]. Although numerous articles have been published on the optimization of CL structure by numerical models, less experimental investigations are available [17, 25, 26]. Due to the involvement of numerous CL parameters which are interdependent it is difficult to obtain a clear picture of the influence of individual parameters on performance.

Pt catalysts dispersed on solid low surface area carbon (SC) support have higher ECSA but lower ORR mass activity than on high surface area carbon (HSC) support in the CL. ECSA retention capacity is higher with increasing porosity. There is a tendency of ionomer to not fill pores smaller than 4 nm [27, 28], and hence the carbon pores ≤ 4 nm are very critical [22, 29, 30]. Electrodes should be well-balanced between thickness and porosity. Electrical contact and conductivity are facilitated by thin electrodes, but at the expense of porosity and vice

versa [31, 32]. Thickness and high tortuosity of electrodes is inversely proportional to the proton conductivity. Optimized humidification of electrodes reduces the O_2 diffusion resistance. However, Park et al. [33, 34] stated that the excessive swelling of the ionomer causes larger O_2 diffusion resistance. The average thickness of ionomer over catalyst particles or agglomerates in commercial electrode is 6 - 14 nm [10, 16, 35, 36]. Thinner ionomer layers than 4 nm are associated to a laminar bilayer with reduced proton conductivity [37]. Regarding platinum loading, the lower the Pt content the higher the ionomer:Pt ratio. Shashikumar et al. [41] showed that ionomer loading should increase as Pt loading decreases to maintain high performance. In their experiment using electrodes with 0.5, 0.25, and 0.1 $mgcm^{-2}$ Pt-loading, the highest performances were achieved at 20, 40 and 50 wt.% loading of ionomer, respectively. Ionomer to carbon (I/C) ratio should be the same for all kind of carbon content. Especially, the proton resistivity of the cathode has strong dependency on the ionomer at lower I/C ratio. It is reported that oxygen transport resistance through the ionomer coating over Pt/C agglomerates is a rate determining step of the CL activity [10, 16]. Moreover, it is proposed that limitations of the oxygen transport through the ionomer can be mitigated by decreasing the ionomer film thickness, and increasing the thickness of CL. Nevertheless, expanding the porosity of the CL, reducing the ionomer thickness and employing thicker CL reduce the effective proton conductivity. This causes inadequate proton conductivity, and possibly also non-uniform potential distribution in the CL leading to accelerated local degradation. Considering this phenomenon, an effective strategy would be to increase the permeability of oxygen in the ionomer to maintain satisfactorily high cell voltages at high current density with lower loading of Pt [32, 42-47]. generally, it can be stated that high performance of MEAs have been achieved by empirical variation of coating parameters but a rational approach in this regard is still missing.

In this work, CLs were fabricated using different coating techniques: dry-spraying [48, 49], airbrush [50-52], screen-printing [53, 54], doctor-blade [55], drop-casting, inkjet-printing [56, 57] yielding different microstructures that were determined using focused ion beam electron microscopy (FIB-SEM) and atomic force microcopy (AFM). Moreover, the MEAs were characterized electrochemically to understand the relation between electrochemical performance and microstructure. In this context, MEAs with same Pt loading were produced by means of same drying procedure for wet methods, and tested in same operating conditions. A drastic variation in the performances was observed when characterizing the MEAs electrochemically, where the only difference among them is the coating method. Clearly, a single property, e.g. ECSA, does not suffice to evaluate CL performance due to the complexity of interactions. This work does not aim at providing a high performance of an individual coating technique but aims at providing a link between electrochemical behavior and microstructure and uses the different coating techniques to prepare CLs with diverse properties. This article demonstrates how different coatings results in different microstructures of CL and influence the transport and charge transfer limitations.

2. Materials and Methods

2.1 Ink and Electrode Preparation

All MEAs prepared in this study are symmetrical, i.e. they consist of identically prepared anode catalyst layer (ACL) and cathode catalyst layer (CCL). However, as the loading on anode is relatively high (0.2 ± 0.02 mg cm^{-2}) the contribution of the ACL to performance limitation are neglected [58]; i.e. only the contributions from cathode dominate the overpotentials. The CLs were prepared by different coating techniques either as CCMs or as GDEs. The specification

of the MEAs along with recipes of the individual catalyst suspension are summarized in Table 1. Moreover, the table contains ECSA determined from CV measurement (see Figure S1 in the supporting information) as well as the electrode thickness determined from SEM cross sections (see Figure S2 in the supporting information). It is worth mentioning that the ECSA values demonstrated in this study are below literatures values [59, 60] because the used coating techniques were not fully optimized as state of the art. The reduction of ECSA of the inkjet and the dry spray sample is caused by Pt agglomeration observed by SEM (see Figure S3). In case of the drop casted GDE a particularly strong penetration of the catalyst suspension into the GDL is confirmed by EDX (see Figure S2 and Tables S1-S4). Typical ECSA values for CL with 0.20 $mgcm^{-2}$ are in the range 40-80 $m^2\ g^{-1}$ according to literatures [61-64]. The ECSAs reported here are in the range 12-57 $m^2\ g^{-1}$; the covered ECSA range is broad and therefore allows to analyze the impact on performance properly.

For the preparation of catalyst inks or powders bath sonicator ELSER 60 Hz, and a probe sonication device UP200S from hielscher, a Cryogenic mill from 6850 Freezer Mill, spex as well as a ball mill from Fritsch-Pulverisette 7 with Zirconia ball was used. Hot pressing was applied using a Vogt device.

Catalyst powder (HiSPEC 4000 with 40 wt% Pt from Johnson Matthey) was purchased from Fuel Cell Store, and Nafion® XL membrane (28 µm) as well as Nafion® ionomer (5 wt. % dispersion in alcohol-water, eq. wt 1100 g/mol SO_3) were obtained from DuPont. For all MEAs the gravimetric catalyst-to-ionomer ratio (catalyst corresponds to Pt/C) was kept at 70:30, whereas the ionomer-to-carbon ratio was 0.71. Other solvents like HPLC grade ultra-pure (U.P.) water, glycerol, isopropanol were purchased from VWR. H_2 and N_2 gases were purchased from Linde, and compressed air was used after filtration from an in-house compressor. Gas diffusion layers (GDLs) are 25BC Sigracet® from SGL Carbon. Teflon gaskets

(205 µm) were purchased from Bohlender. Individual solvent amount is calculated from the weight-based mass ratio with catalyst (Cat). The Pt loading for anode and cathode catalyst layer equals to 0.20 ± 0.02 mg cm^{-2} in each MEA as confirmed gravimetrically.

Table 1: Summery of the MEAs prepared using different coating techniques for anode and cathode CLs.

Method	MEA type	Solvent 1	Solvent 2	Mixing process	Electrode thickness/ µm	ECSA / $m^2 g^{-1}$
Dry spray	CCM	None	none	Cryo-mill, knife mill	6.5 ± 2.2	15
Air brush	GDE	UP water: Cat × 100	Isopropanol: Cat × 100	Ultrasonication	8.8 ± 2.2	57
Screen printing	GDE	UP water: Cat × 5	none	Ultrasonication, roller ball mill	9.0 ± 3.7	48
Doctor blade	GDE	UP water: Cat × 3.75	Isopropanol: Cat × 1.75	Ultrasonication	7.0 ± 0.7	42
Drop casting	GDE	UP water: Cat × 118	none	Ultrasonication	3.2 ± 0.8	16.5
Inkjet printing	GDE	Isopropanol: Cat × 60.8	Glycerol: Cat × 13.33	Ultrasonication	3.0 ± 0.7	12

It is worth mentioning that every ink dispersion media is adapted to their individual coating techniques resulting in slight changes of solvents, see Table 1. It is a requirement for individual coating techniques, as each coating techniques handles different viscosities of ink. Major properties of the different CL preparation techniques, which are used in this study, are provided in the supporting information. The optimization of each technique was not within the scope of this work. GDEs were prepared in all cases except from the dry spray as it only allows membrane as substrate [49].

2.2 MEA Processing

Apart from dry sprayed CCMs, all the other GDEs are furthered dried in a drying oven at 70 °C for 6 hours. After preparation of the catalyst layer the MEA components were assembled by 5 minutes hot pressing at 140 °C and at 650 N cm^{-2}. Two sets of MEAs were prepared by each coating methods and characterized. All fuel cell tests were performed with a commercial cell from ElectroChem. Inc., which is made of two graphite plates with flow-field (see Figure S4 in the supporting information) and a pair of gold coated stainless steel as current collector. Cell specifications are stated in Table 2. One of the most important factors in the assembly of PEMFCs is to set the appropriate compressive stress to the cell to balance the conflicting demands of mitigating gas leaks and decreasing contact resistance without damaging the porous components [65]. The amount of compression on the GDL affects the contact resistance, the GDL porosity, and the fraction of the pores occupied by liquid water, which, in turn, affect the performance of a PEMFC [66]. After hot pressing a 20 % compression in the gas diffusion media was determined by measuring the thickness of MEA before and after the hot-pressing.

2.3 Physical Characterization

Scanning electron microscopy (SEM): To observe the surface of the CCLs with scanning electron microscopy (SEM), specimens were prepared by cutting approximately 0.3 × 0.3 cm^2 from GDE or CCM. The surfaces of the samples are carefully installed with a carbon tape in the SEM sample holder. The measurements were carried out with a Zeiss UltraPlus, providing an electron beam of 5 kV that allows the analysis of the surface without destroying the ionomer. EDX measurements were, however, done with a higher accelerating voltage of 15 kV as this is

needed for quantification of heavier elements such as platinum. For EDX mapping ion cut samples were prepared using an Jeol ion cut polisher (Ion cutting system JEOL IB-19520/CCP, used with Argon gas) with 6 kV for 6 h for each sample while swinging the sample stage during the cutting process. The EDX mapping and imaging of the cuts were performed with a JEOL field emission microscope (JSM-7200F) with Schottky-Emitter with a Bruker Quantax Energy dispersive X-ray system (Quantax XFlash6/60) at 15 kV.

Focus Ion Beam Scanning Electron Microscopy (FIB-SEM):

After electrochemical characterization of the MEA, the MEAs were delaminated manually and samples were cut into squares of 0.5 × 0.5 cm^2 After placing the sample (in all cases the CCL stickling on the membrane was used) inside the FIB-SEM sample holder, the fracture was made by emerging the sample into liquid nitrogen. Measurements were carried out at 1.5 KV EHT with a 30 KV FIB probe. By 20×20 µm cut area the measurements were performed with standard image resolution of ~20 nm/ pixel. The thickness of each cut is 150 nm. The FIB-SEM images were taken with a Zeiss scanning electron microscope (Neon 40 ESB Crossbeam).

Atomic Force Microscopy (AFM):

AFM measurements were carried out using a Multimode 8 AFM (Bruker) with Nanoscope V controller. Conductive tapping, while averaging the current over the whole cycle (TUNA current) or over the time in contact with the sample (contact current) with a lock-in amplifier, was performed (PF-TUNA, Bruker) on the surface of the catalyst layers. The GDEs or in case of the dry sprayed catalyst layer a CCM were cut in pieces of approximately 0.5 x 0.5 cm^2. The samples were glued to 12 mm AFM steel disks using conductive tape (Plano) underneath and near the measuring spot. In addition, nanomechanical properties, like adhesion, deformation

and stiffness were recorded simultaneous. More information on AFM measuring conditions are provided in the supporting information. Generally, AFM analysis allows to distinguish:

- An area in which the adhesion or deformation is high but the TUNA current is low (shown in red) which corresponds to the ionomer.
- An area in which the TUNA current was visible and the adhesion or deformation are high (shown in grey) which is interpreted as thin or non-covering ionomer layers
- An area in which the adhesion and deformation have low values (shown in black) which is characteristic of Pt/C

2.4 Electrochemical Characterization

Single cell test: The MEAs for single cell characterization were tested in an in-house developed test bench. The test bench has two bubbler humidifiers for both anode and cathode gas inlet; moreover, the pressure of the system is controlled at cell outlet. The cell exhibits a pressure drop of 5-8 mbar at 70 ml min^{-1} and 1500 mbar pressure on the cathode side The MEA test specifications and operating conditions are stated in Table 2. Each MEA was conditioned at 100 % RH (relative humidity), however all the MEAs were tested at 50 % RH to avoid flooding issues. 1.5 bar absolute gas pressure was maintained in the anode and cathode compartment.

Breaking-in and polarization curve: After starting the test bench each MEA was conditioned in potentiostatic mode at 0.6 V for 1 hour at 100 % RH. Subsequently, humidification was reduced to 50 % RH and further operation was performed in galvanostatic mode for 6 hours with a stepwise increase of current density to 250, 500 and 1000 mA cm^{-2}. Break-in step is

considered completed if voltage change is lower than 10 mV h^{-1} at a current density of 1000 mA cm^{-2}. Polarization curve was recorded using an electrical load (Hoecherl and Hackl GmbH) in galvanostatic mode. The cell voltage was monitored using a dwell time of 3 min for each current increment which was 25 mA cm^{-2} in the range 0 to 100 mA cm^{-2} and 100 mA cm^{-2} for current densities above 100 mA cm^{-2}. Two sets of data have been recorded for each measurement, and the average value has been used.

Impedance Analysis: Electrochemical Impedance Spectroscopy (EIS) was performed for all MEAs using Zahner Zennium with PP241 Load. The equivalent circuits are simulated by the Thales software from ZAHNER-Elektrik GmbH & Co. KG. Nyquist and Bode plots were determined within the frequency range from 100 mHz to 100 kHz in three different current densities at 0.1, 0.5 and 1 A cm^{-2} with appropriate (5 to 10 % of current) amplitudes. The measurement regime was linearized by stabilizing the cell for 10 minutes prior to EIS measurement. Anode functions as a reference and counter electrode, whereas cathode acts as a working electrode. Nyquist plots are formulated with the real impedance in the X axis and imaginary impedance in the Y axis.

Table 2: MEA test conditions and cell specifications

Operating conditions and specifications for the single cell test facility			
Teflon gasket thickness			205 micron
MEA compression within bipolar plates, 5mm screws 4 pieces			2 Nm each
Flow channel (Graphite)			Two inlet points and triple channel serpentines
Active area			1 cm^2
Anode stoichiometry	1.6	Cathode stoichiometry	2.5
Anode outlet pressure	1.5 bar absolute	Cathode outlet pressure	1.5 bar absolute

Anode humidification	50 % RH	Cathode humidification	50 % RH
Humidifier temperature, cell inlet temperature			80 °C, 85 °C
Cell temperature			80 °C

Ionic Conductivity: The ionic impedance of the electrodes was also evaluated by EIS using electrochemical test stations from ZAHNER-elektrik GmbH & Co. KG. In order to characterize ionic impedance, 12 ml min^{-1} of nitrogen and hydrogen gas were fed into cathode and anode with 100% humidification. To avoid the contribution from ORR charge transfer, cathode compartment is purged with nitrogen during the measurement. Consequently, the charging of the catalyst's double layer with the ionic resistance of CL becomes dominant. Ionic impedance was measured in 1 V potentiostatic condition with 10 mV amplitude from 500 mHz to 100 KHz frequency. A Warburg-like response (45° slope) is observed at high frequencies, corresponding to the ionic conductivity (both for electron and proton) in the catalyst layer [67, 68]. At low frequencies, the impedance plot curves up to a limiting capacitance response (vertical) which corresponds to the total capacitance of the catalyst layer. The ionic resistance, R_{ionic}, can be obtained from the length of the Warburg-like region projected over the real impedance (Z´) axis (= $R_{ionic}/3$) with the aid of a transmission line model. However, in our work not all electrodes corresponds to the 45° slope likely due to an inhomogeneous thickness of the electrode and ionomer distribution (see Figure S5 in the supporting information)[67].

Cyclic Voltammetry: Cyclic voltammograms (CVs) were obtained at 1.5 bar absolute pressure and 80 °C with 20 mV s^{-1} slew rate between 60 mV to 1 V. The electrochemical active surface area for each of the cathodes can be measured by calculating the adsorption (used in this work) or desorption of the hydrogen on Pt surface. To measure cathode CV of H_2 and N_2 gas (each 12 ml min^{-1}) were fed with 100 % humidification to anode and cathode, respectively. The coulombic charge for hydrogen desorption was used to calculate the active surface area

of platinum considering the charge needed to adsorb or desorb a monolayer of H^+ on polycrystalline platinum [69]. Thereupon it is possible to obtain the electrochemical surface area (ECSA) of the cathode through $ECSA=q_{Pt}/(\Gamma \cdot L)$, where, q_{Pt} is the charge density (C cm^{-2} electrode) obtained from the CV experiment, the charge required to reduce a monolayer of protons on Pt, Γ = 210 µC cm^{-2}, and the Pt content or loading in the electrode, L, in g_{Pt} cm^{-2}. The charge was determined from the CV plot by extrapolating the capacitance curve/line through the desorption peak from 60 mV to 400 mV.

3. Results and Discussion

3.1 Electrochemical characterization

Current-voltage (I-V) polarization and performance curves obtained using the different MEAs are plotted in Figure 1 (A) and (B), respectively. The open circuit voltages (OCV) are around 900-920 mV. With slightly increasing current density (up to 0.05 A cm^{-2}) the differences of the performances become obvious in the inset of Figure 1 (A) due to very different kinetic activity of the MEAs. Clearly the airbrush electrode shows the lowest kinetic losses; according to Table 1 it also exhibits the highest ECSA. Drop casted MEA and inkjet printed MEA, on the other hand, exhibit high kinetic losses. Even though performances of drop cast and inkjet printed MEAs are substantially lower in the kinetic region than the one of dry sprayed MEA, the ECSAs of these three MEAs are very similar. This clearly suggests that ECSA is only one factor determining electrode kinetics. The inkjet printed MEA, which has lower performance than the dry sprayed MEA in the kinetic regime, has a lower slope in the linear region > 0.5 A cm^{-2} and therefore outperforms the dry-sprayed MEA for current densities > 0.75 A cm^{-2}. This behavior was also reported by the Shukla et. al. for other inkjet printer MEAs [70].

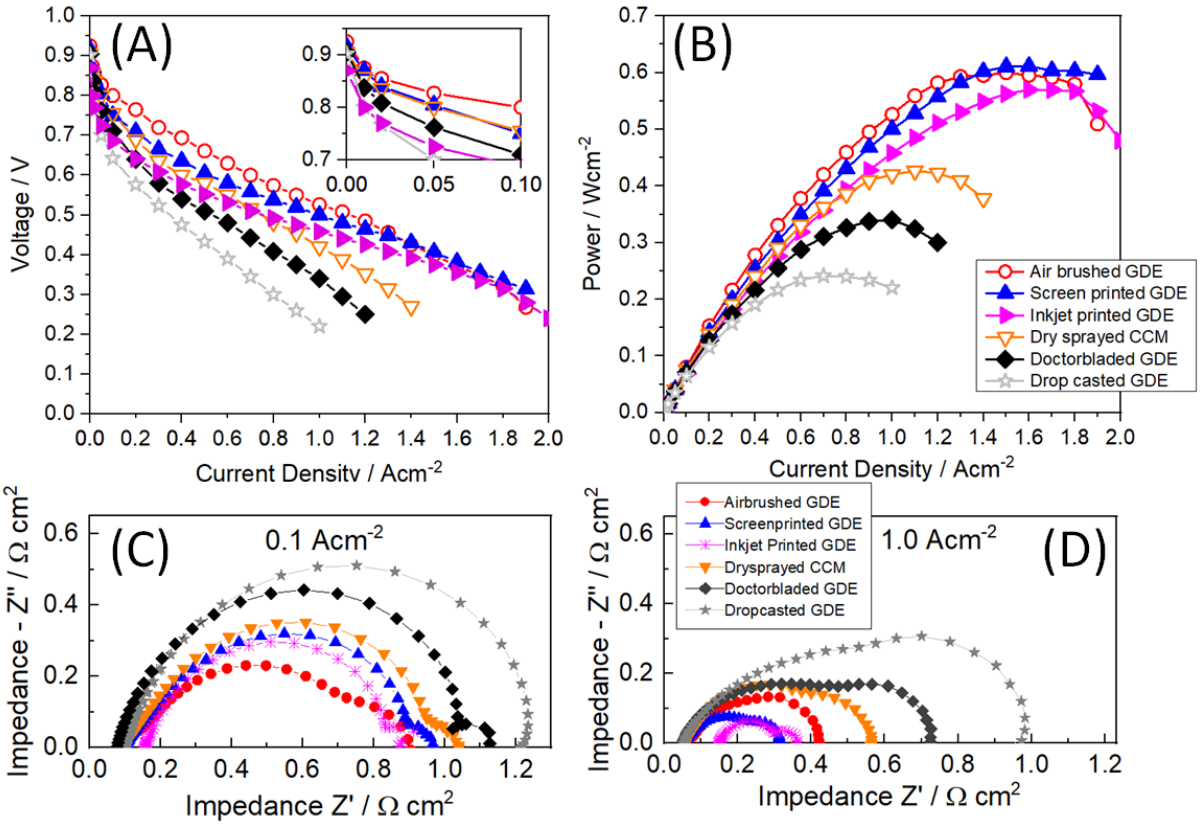

Figure 1: (A) I-V curves of the different MEAs prepared with different coating methods. (B) Power curves of the different MEAs. The Pt loading of the CCLs is 0.20 mg cm^{-2}. The tests were performed at 80 °C, 50 % RH of H_2 and air, 1500 mbar absolute pressure at the anode and cathode and stoichiometries of $\lambda_{H2} = 1.6$, $\lambda_{oxygen} = 2.5$. (C) and (D) are nyquist plots of the different MEAs recorded at 100 mA cm^{-2} and 1 A cm^{-2}, respectively.

The MEA prepared using doctor-blade shows poor performance in kinetic region as well in ohmic region. At high current density >1.5 A cm^{-2} airbrushed, screen-printed and inkjet-printed MEAs show largely linear characteristics; all other MEAs suffer ohmic and substantial mass transport losses. According to power density curve in Figure 1 (B), drop-casted MEA shows very poor performance all along. Due to fast kinetics of the anode catalyst layer (for all MEAs anode CL is identical to cathode CL) the observed losses are clearly ascribed to the cathode catalyst layer.

In addition to I-V curves, EIS analysis was performed to provide complementary information on the different contributions to the voltage loss. Figure 1 (C) displays Nyquist plots at low current density (0.1 A cm^{-2}), where the kinetics overpotential is dominating. Figure 1 (D) demonstrates a Nyquist plot at high current density (1 A cm^{-2}) with predominant mass transport limitations. At low current density a small contribution of anode activation is distinguishable at around 10 kHz when the arc due to charge transfer resistance of the cathode is small and does not overlap with the anode signal (blue and red data). Generally, the first big semi-circle is indicating kinetic impedance and clearly highlights the catalyst performance of the electrodes. Larger kinetic impedances can be explained by lower Pt utilization leading to lower effectiveness of the catalyst layer. This phenomenon suggests that even though we have a nominally the same Pt loading in all electrodes, the access to Pt surface is different due to different microstructures resulting from different coating methods. Differences can be related, for instance, to ionomer distribution in the catalyst layer as well as to porosity. At high current density (Figure 1 (D)), the second semi-circle becomes clearly visible, which is caused by diffusion related impedance originated from CCL and GDL [71, 72]. Interestingly the inkjet-printed MEA shows the lowest diffusion impedance, which is also reflected in a relatively high performance at high current densities. However, in both Figure 1 (C) and (D), inkjet-printed electrode shows a very high ohmic resistance (X axis intercepts at high frequency) which might be due to poor electrical contact at the interfaces. The relatively low slope of the polarization curve observed at > 0.5 A cm^{-2} in Figure 1 (A) indicates that mass transport resistance and kinetic charge transfer are particularly low for the inkjet printed MEA. On the other hand, dry sprayed, doctor bladed and drop casted GDE display increasingly larger arcs related to mass transport losses, which is expected as the I-V curve exhibit high slopes at higher current densities.

A single model concept was used to fit the EIS data using an equivalent circuit (E.C.). However, two complementary equivalent circuits were used; one representative for low and another representative for high current densities as shown in Figure 2. In both cases, the first component is an inductor which represents the influences of wiring. The next element of the E.C. is a resistance, which represents ohmic losses of the experimental setup. At low current density, a small contribution from anode charge transfer and no significant diffusion limitation is expected. Figure 2 (A) shows the E.C. used for low current density where ohmic resistance (indicated as orange) along with cathode charge transfer resistance (indicated as turquoise blue), represented by a RQ (resistance with constant phase element) element, dominate. The individual phase angles (α values) are indicated inside the bars.

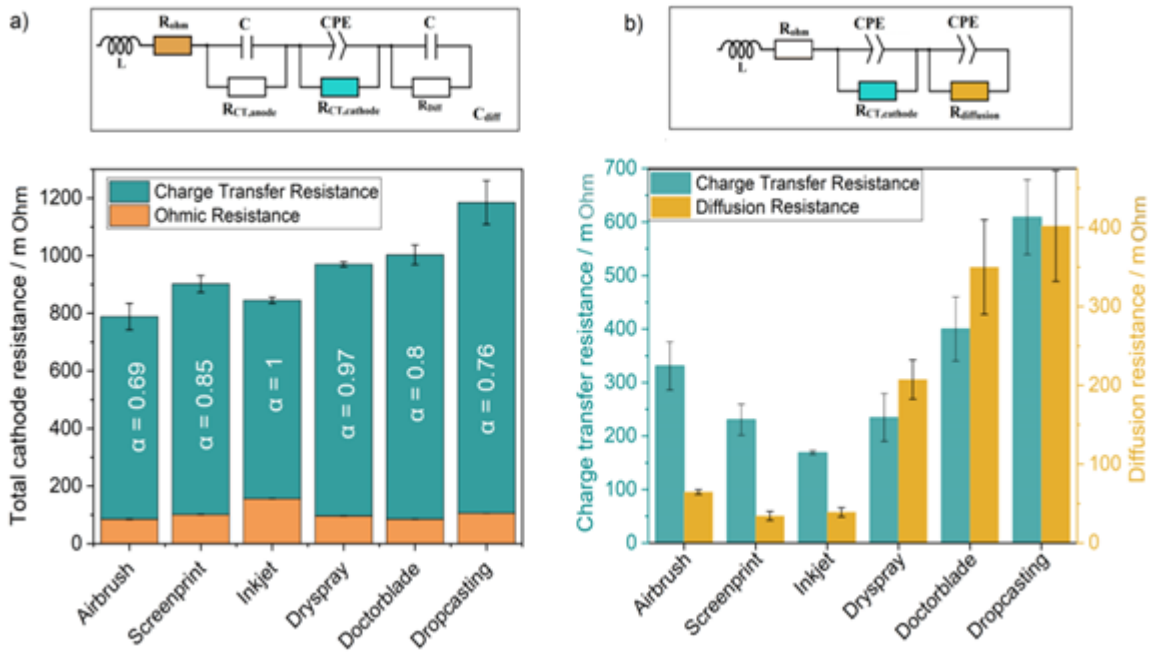

Figure 2: Evaluation of EIS analysis using the equivalent circuit shown at the top of the figure. (A) Added-up values of the ohmic resistance R_{ohm} and charge transfer resistance R_{CT} determined at 0.1 A cm^{-2}. The phase angle of the CPE, α, is depicted in the bar. (B) Charge transfer resistance and diffusion resistance determined at 1 A cm^{-2}. The error bars correspond to the fitting error attributed to the individual component.

The anode kinetics and concentration loss, which are very limited in this domain are represented with simple RC (resistance with capacitance) element. A RC element also has been integrated to simulate diffusion. At high current density the anode contribution is negligible due to the dominating cathode charge transfer and mass transfer effects. Hence, the first RC element (for anode charge transfer) is eliminated from the E.C. as shown in Figure 2 (B). However, due to higher diffusion resistance at high current density, a diffusion element (RQ) is used in series together with the RQ circuit that represents mass transfer. Such E.C. with a diffusion element is necessary to understand transport limitations of differently prepared electrodes at high current density. Error bars determined in the fitting from individual component in the E.C. are given in the figure. At low current density, ohmic resistance and cathode charge transfer resistance contribute most significantly to the voltage losses. Aside from the inkjet printed CCL, a gradual increase in charge transfer resistance from airbrush to drop casting is observed. From polarization curves and Nyquist plots it is assumed that, even though the performance of the inkjet printed MEA is poor in the kinetic region, it drops only slowly with increasing current density due to the superior charge transfer properties of the cathode. The same phenomenon is observed by comparing both E.C. simulations in Figure 2 (A) and (B). For inkjet printed electrode alpha = 1, which suggests an ideal RC (with capacitance) element, and the charge transfer resistance is lowest compared to electrodes prepared with other techniques. On the other hand, the E.C. at high current density demonstrates slightly different trend. Screen printed, inkjet printed and airbrushed MEAs show particularly low diffusion resistances. However, the diffusion resistance increases drastically from screen/inkjet printed MEA to doctor bladed MEA and finally reaches the highest value in case of the drop casted MEA. Besides, the RQ element attributed to the charge

transfer overpotential shows that the dry-spray and the screen-printed MEA exhibit an analogous resistance, which are lower than airbrushed MEA. Here, electrode prepared with the inkjet printing method exhibits the lowest charge transfer resistance. It can be speculated that the higher values of diffusion resistance in dry spray, doctor blade and drop cast MEA is due to the larger agglomerates and ionomer films formed during coating.

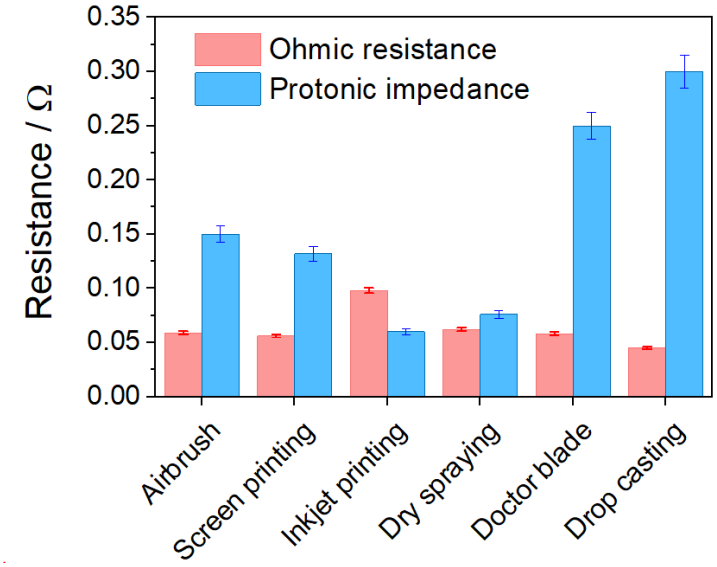

Figure 3: Bar chart of ohmic and protonic impedance of different catalyst layers determined from EIS spectra in H2/N2

Ionic conductivities and ohmic resistances of the studied CCLs determined from EIS spectra in H_2/N_2 are depicted in *Figure 3*. It is noted that proton conductivity values need to be taken with care, since several spectra do not exhibit the typical Warburg like shape (see Figure S5 in the supporting information). The drop casted CCL shows the lowest ohmic resistance, since it is prepared directly from a single layer and exhibits low interfacial resistances. Furthermore, proton conductivity is high in case of airbrush and screen-printed CCL, whereas inkjet-printed and dry sprayed CL show the highest proton conductivity through the electrode. On the other hand, doctor bladed and drop casted CCLs exhibit very low protonic conductivities.

3.2 Investigation of CCL structure

3.2.1 SEM and AFM analysis

In this work, each fabrication method uses different solvents or solid-solvent ratio, likely leading to slightly different ionomer-catalyst-solvent interactions which causes very different structure of the CCLs. Cross sections of CL samples prepared using ion cutting and measured using SEM/EDX are presented in Figure 4. The measurement of the uncoated GDL is provided in the supporting information for comparison (Figure S6); it apparent that the used GDL substrate exhibits strong inhomogeneities regarding the thickness of the MPL.

The airbrushed CL shows the largest thickness along with the screen-printed CL. Besides some accumulation of catalyst ink on top of the layer its appearance is homogeneous while the thickness of the screen printed GDE varies to a large extend. Interestingly at an area of approximately 20 µm a higher fluorine contend was measured for the screen printed GDE in the MPL. The layer thickness for the CL done by inkjet printing is smallest while it was confirmed by EDX that the ink must have penetrated the MPL (Table S3 in the supporting information). Also, a high amount of platinum agglomerates was imaged. The dry sprayed sample does not show the common appearance of an CL. Large carbon/ionomer particles are imaged, with platinum at the outer shell. The line-scan in Figure S2 confirms this observation. As can be seen in the inset of Figure 4 (D) the large carbon/ionomer agglomerates seem to have a porous structure. For the sample prepared with drop casting a large amount of platinum was measured in the GDL part of the CL (Table S4). The CL produced by doctor blade showed a homogeneous layer thickness with no signs of a far penetration of the ink components into the MPL.

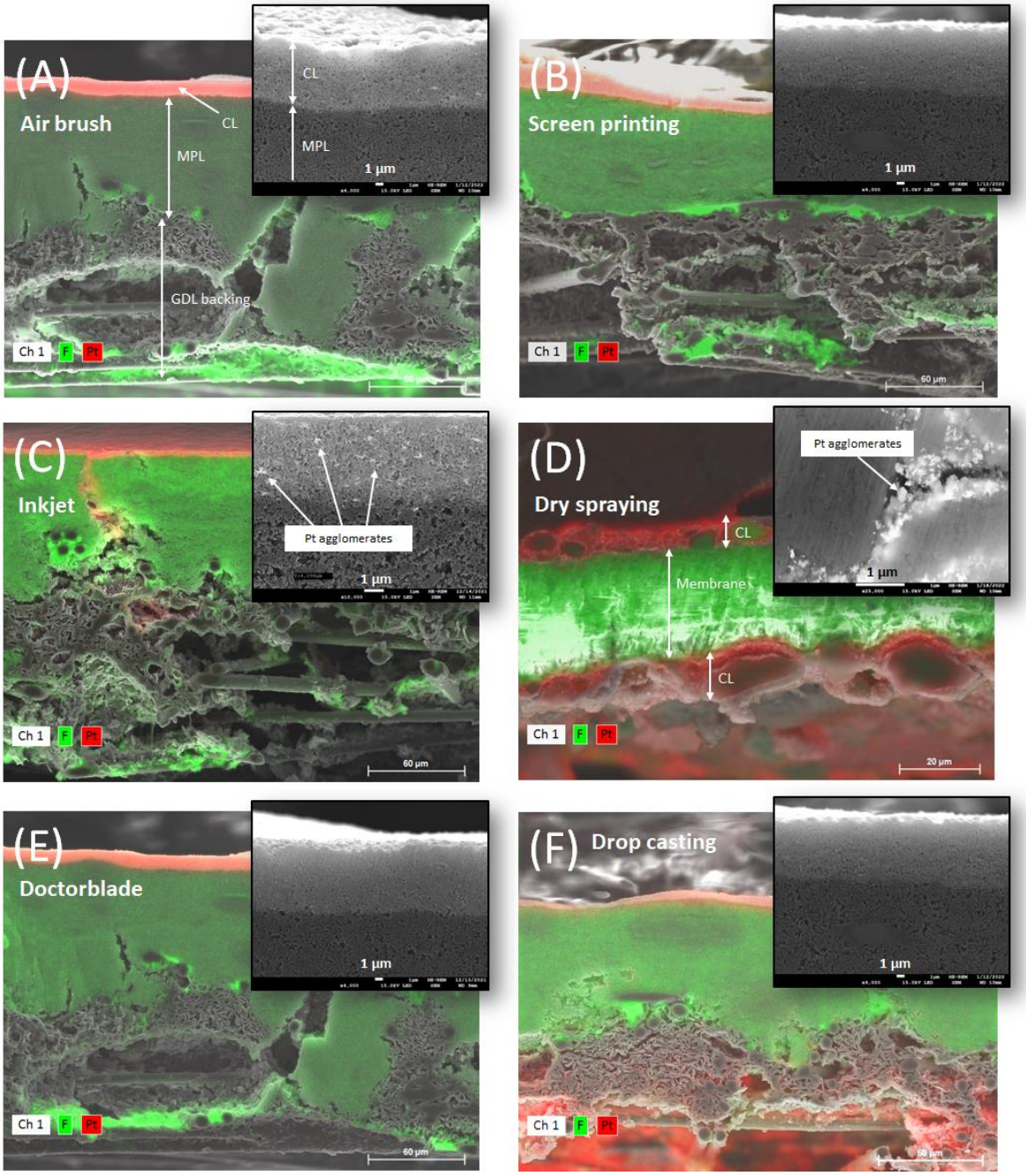

Figure 4: SEM/EDX cross sections (ion cut) of the investigated GDEs (A)-(C), (E) and (F) a CCM in case of dry spraying (D). The insets show enlarged view of the CLs and the CL/MPL interfaces. In case of dry spaying enlargement of the inner CL structure is shown.

In Figure 5 top view SEM images (1st row) and AFM images of the CCL surfaces are shown. The AFM images show height measurements over a large area of 2500 µm² which represents the topography of the samples (2nd row), as well as a combination of adhesion measurements which reveal the ionomer distribution in the catalyst layer with the current distribution (3rd row). The segmentation was done with an algorithm that compares the nanomechanical and nanoelectrical information pixel by pixel. A high adhesion or deformation (only adhesion is shown) corresponds typically to ionomer in contrast to low deformable and low adhesive catalyst. When no electronic current was measured the ionomer was thick enough or dense to withstand the AFM tip, which is shown as thick ionomer layer. These thick ionomer layers shown in red thus represents the areas where no electronic current was measured and the adhesion was high. Actual thickness values cannot be interpreted from these surface measurements, nevertheless it is reasonable to explain this behavior as follows: When the same ionomer volume was used and there is less ionomer area visible, then the layers have to be thicker in comparison to CCLs in which a higher ionomer area was measured on the surface. So, ionomer counted as thick can still be thin, but the terminology is used to distinguish these from the areas described as follows. Areas with low adhesion or deformation were treated as catalyst. A thin or less dense ionomer layer can be pushed through or besides when operating the AFM in tapping mode, i.e. the AFM tip gets an electronically conductive connection with Pt/C. Thus, areas with high adhesion or deformation and electronic current were counted as thin ionomer layers (shown in grey). Still, the adhesion and current are affected by the ionomer layers as the contact area of the AFM tip changes due to the ionomer. Another effect for these areas cannot be excluded. It is noted that the main assumption when interpreting the AFM images in Figure 5 is that a well dispersed areal distribution of these three different areas leads to superior performance whereas dominance of one area type and

coarse distributions lead to inferior performance. This particular assumption is true in case of airbrush and screen-printed CCL as shown as bar chart in Figure 6 (A). The SEM image of airbrush CCL, shown in Figure 5 (A), clearly exhibits a very porous electrode, which however, also consists of a few random agglomerates. When the solvent does not completely evaporate during the spraying process before reaching the substrate, these types of agglomerates could form. The topography measurements with AFM represents the nanostructure which shows a high number of pores with different sizes comparable to those of the SEM measurements. According to AFM data the CCL prepared using the airbrush coating method yields a superior ionomer distribution with a high number of high adhesive and low electronically conductive areas and still a fair amount of electronic conductive area, which means homogeneous distribution of thin film of ionomer throughout the CCL visible in the combined AFM measurement in the 3rd row. Figure 5 (B) demonstrates a CCL prepared with screen printing, which shows a smooth surface but with large cracks in the CCL seen in SEM images. The smooth CCL prepared with the inkjet printer is shown in Figure 5 (C) which gives a comparable structure to the screen printed CCL but without cracks visible in SEM images. In addition, the CCL printed with inkjet shows a reasonable conductive area but a lower total ionomer coverage compared to airbrush and screen-printed CCL, thus thicker ionomer layers. Very rough and agglomerated surfaces of individual aggregates is shown in Figure 5 (D) for dry-sprayed samples. We assume every secondary particle is a mixture of Pt/C and ionomer in this case. However, due to spraying of solid powder, large agglomerates of > 1 µm become visible. The ionomer within these agglomerates seems to be reasonable distributed but may result in a high ionic contact resistance between the agglomerates as there will be no continuous path of ionomer layers through the CCL. The contact resistance between large agglomerates might add to the overall electronic resistance. Figure 5 (E) depicts a doctor bladed CL surface, which

looks quite homogeneous besides some small cracks. In general, a compact layer is evident (i.e. larger structures of several microns are not visible). The total ionomer area is relatively low, which is an indication for thicker ionomer layers or agglomerates, as the same amount of ionomer was used in all samples. This is expected to add to a high oxygen diffusion resistance and less connected ionomer and thus a high ionic resistance. The CCL prepared with doctor blade in Figure 5 (E) has a rather heterogeneous distribution which is caused by a high percentage of areas of Pt/C with no ionomer coverage corresponding to a poor ionomer distribution. Apparently, this localized and uneven distribution of areal classes in the CCL causes poor performance to the doctor-bladed CCL. Figure 5 (F) shows a very compact CL prepared with the drop-casting method. Drop casted CCL shows low ionomer coverage which causes inhomogeneous distribution throughout the CCL leading to a poor performance. These last two methods have in common that they consist of a single compact coated layer. This phenomenon is clearly highlighted by the high diffusion resistance of doctor blade and drop casted electrodes. Nevertheless, electronic conductivity measured by AFM was highest for these two layers which will be discussed in more detail later. Note that the effect of the macroscopic cracks in the MPL or CCL is out of scope of this study and we assume that it does not influence performance to a significant degree.

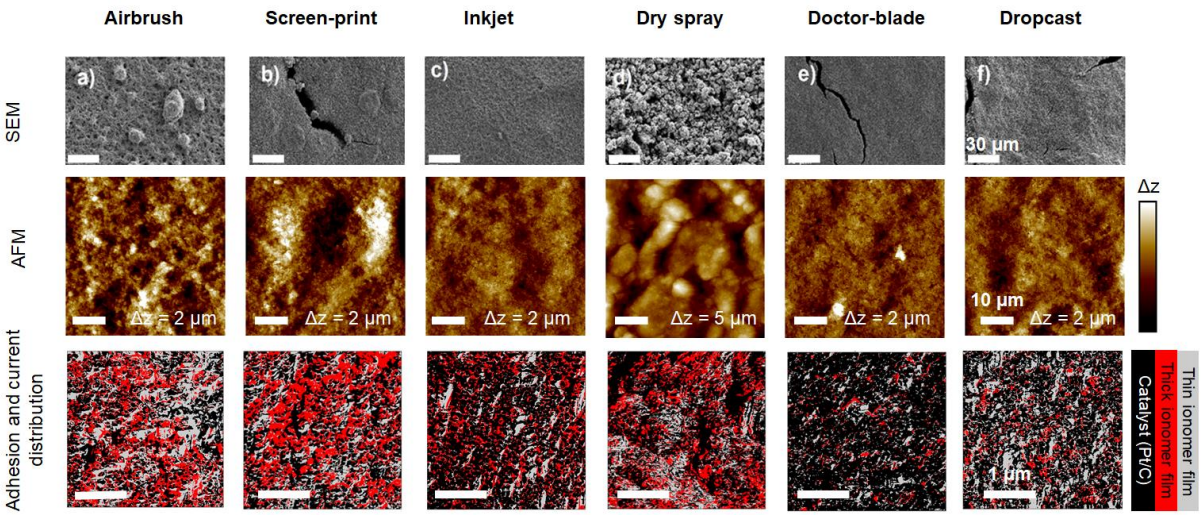

Figure 5: SEM and AFM images of 6 different pristine catalyst layer surfaces prepared through individual coating methods. The first row shows the SEM images with 500 x magnification; the white scale bar represents 30 µm; the second row are the topographic distributions from the AFM measurement at a scale of 50x50 µm² (scale bar represents 10 µm); third row shows the segmentation result of adhesion and TUNA current distribution throughout the CL surface with a scale of 3x3 µm² The columns correspond to a) airbrush, b) screen print, c) inkjet print, d) dry-spray, e) doctor-blade, and f) drop-cast.

In order to analyze the ionomer distribution in the CCLs in more details Figure 6 (A) show the percentage of areas corresponding to thick ionomer layers, thin ionomer layers and areas without ionomer coverage. Figure 6 (B) shows the roughness of the electrodes derived from 50x50 µm² measurements. The data was derived from the adhesion, electronic current and morphological study of AFM measurements shown in Figure 5. The values for segmentation were derived from line analysis between catalyst particles and ionomer phase. We consider similar areas with good distribution to be the main indicator of superior performance (similar size of the three bars in Figure 6 (A)). On the contrary, a dominating area for electronic conductivity is indicative of inferior performance (large difference of heights of bars in Figure 6 (A)). High adhesion values in addition with no electronic current shows a full coverage of

Pt/C (orange bar “thick ionomer film”). A very thin or even partially covering ionomer layer is plotted as a green bar (“thin ionomer film”). The best performing MEAs have a comparable amount of all areal types. The worse performing MEAs have a high uncovered Pt/C surface (violet bars) (high electronic conductive area and less ionomer) which is indicative of heterogeneous distribution. As a consequence, samples with dominating uncovered Pt/C surfaces can be expected to possess thicker ionomer layers which may be less connected and show a higher resistance for oxygen transport. Additionally, Figure 6 (B) shows the topographic properties of the CL by plotting R_z, R_a and R_q of the different CCLs prepared with diverse coating methods. R_z specifies the maximum vertical distance between the highest and lowest data points of the CL, R_a is the average roughness, and R_q is the root mean square average of height deviations taken from the mean data plane. Apparently, there is no correlation between roughness properties and performance. For instance, the least and the highest performing MEAs prepared using airbrush and drop cast, respectively, show very similar roughness.

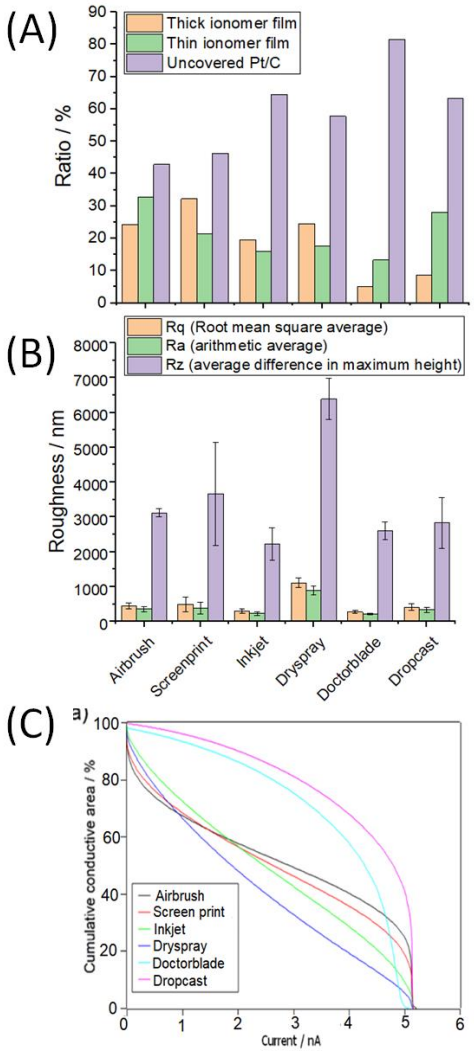

Figure 6: (A) CCL surface properties in terms of ionomer coverage determined usig AFM, (B) Topographic and roughness analysis of CCLs by AFM measurement considering R_z, R_a and R_q values, (C) A contact current plot of AFM tips over the cumulative conductive area of catalyst layers

Another interesting observation from the AFM measurement is provided in Figure 6 (C). When plotting the cumulative area of the conductive CL over the contact current of the AFM tips, an opposite trend to polarization curve series has been found. This may suggest that the poor and inhomogeneous distribution of ionomer (such as for dropcast and doctorblade CCLs) can causes high electric conductivity but inferior performance because of insufficient distribution

of ionomer and Pt/C. The dry sprayed CCL is not following this trend, showing the lowest conductive area over the whole current range. This might be the case as additional resistances in series may add due to the connection between the large agglomerates which are typical for this coating technique. This observation is important as it demonstrates the risk of using a cumulative property for optimizing CCLs. It may lead to an erroneous approach as evidently local resolution and distributions of ionomer and Pt/C is important for the performance. In conclusion, a homogeneous distribution of thick ionomer, thin ionomer and free catalyst surface (electronic conductive path) derived from AFM measurements can be correlated with a high performance MEA. Generally, a homogeneous distribution of the thick ionomer, which means less agglomeration and thinner individual layers (lower diffusion resistance), was found to be crucial for a good performing CCL. A predominant area of free catalyst, thus a high electronic conductivity, was identified for poorly performing MEAs.

3.2.2 FIB-SEM analysis

In addition to the SEM and AFM analysis, the microstructures were further analyzed by 3D reconstruction based on FIB-SEM data. For the 2D image slices from FIB-SEM (see Figure 7 (A) or Figure S7 in the Supporting Information as an example) with a resolution of 19.25 nm were first postprocessed using the open-source software Fiji [73]. The resolution is sufficient to observe secondary pores, but does not allow to investigate primary pores. After elimination of artificial shifts, proper image alignment to 2D image stack and brightness correction, the image data was further processed with GeoDict®[74]. The quality of the image data was then enhanced by application of a smoothening filter followed by a sharpening filter. The 2D data was processed and stored as cuboid voxels (volume pixels). The microstructure reconstruction was then finalized by a binarization procedure using the Otsu method [75] as visualized in Figure 7 (A) or Figure S8 in the supporting information. The resulting binarized microstructure

was then used as an input geometry for GeoDict® to determine effective transport parameters such as porosity, median pore diameter, diffusivity and permeability. This workflow of microstructure reconstruction from FIB-SEM data and subsequent derivation of effective transport parameters was the same for all samples. The drop-casted CCL however was very thin after delamination of the GDL, resulting in an insufficient number of FIB-SEM images for reasonable microstructure reconstruction and was therefore neglected in the further analysis with GeoDict®. For a more detailed description on the derivation of effective transport parameters with GeoDict® it is referred at this point to the Supporting Information.

Figure 7 (B) shows the pore size distributions as determined by GeoDict® for the microstructure reconstructions of the different samples. It is apparent that most pores exhibit diameters in the range from ~200 to 800 nm and are therefore larger as compared to literature values (typically 20-300nm) [23, 76, 77]. At this point it has to be noted that the FIB-SEM analysis is limited to secondary pores in the CL microstructures since the FIB-SEM resolution is not high enough to consider primary pores of less than 20 nm [77, 78] Based on the derived pore size distributions also median pore sizes (D50) were determined as listed in Table 3. By relating the mean free path length ($\lambda_{air}(20°C) = 68nm$) to these median pore sizes one can see that diffusive transport within the microstructures is not anymore fully dominated by Knudsen diffusion ($Kn \to 0$), but resides with $Kn = \frac{\boldsymbol{\lambda_{air}}}{\boldsymbol{D50}} \approx 0.15 - 0.2$ in the transitional regime between Knudsen ($Kn \to 0$) and bulk diffusion ($Kn \to \infty$). This was accounted for in the diffusivity simulations in GeoDict® by determining the effective diffusivity as the harmonic average of the Knudsen and bulk diffusivity (Bosanquet approximation [79]). More details on the determination of the diffusivity are provided in the Supporting Information.

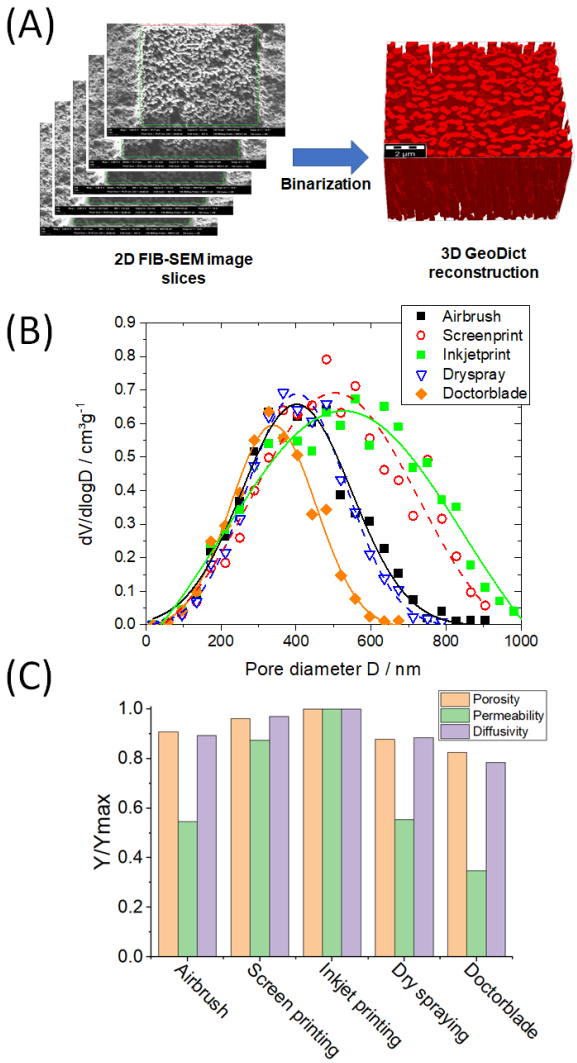

Figure 7: FIB-SEM analysis of CCL microstructures with GeoDict®: (A) Scheme showing 3D microstructure reconstruction via binarization of a 2D greyscale image stack from FIB-SEM. (B) Pore size distributions derived for microstructure reconstructions of the different CCL manufacturing techniques along with Gaussian fits. (C) Effective transport parameters determined for the microstructure reconstructions and normalized by the maximum values among the different CCL samples.

In addition to the median pore size D50 Table 3 also contains all further effective transport parameters, i.e., porosity, diffusivity and permeability. To enhance visibility of trends in those parameters they were furthermore plotted in Figure 7 (C) and normalized by the respective maximum among all samples. Based on this analysis the inkjet sample exhibits the highest overall values, followed by screen-printing. For the airbrush and dry-spraying samples comparable values were derived, leaving the doctorblade CCL as the sample with the least beneficial transport properties. In relating these trends to the I-V curves in Figure 1 it can be observed that the inkjet and screen-printing CCLs achieve for very high current densities the highest performances which can be linked to the lowest mass transport resistance in the CL. However, for lower current densities the trends in Figure 7 (C) cannot be directly linked to the trends in the performance within the i-V curve of Figure 1. This is plausible since in this region gas transport within the pores is not the limiting factor. Another explanation could be that mass transport limitation is caused by another compartment in the fuel cell. Moreover, it seems reasonable that there is a performance bottleneck other than mass transport limitation again highlighting the complexity of parameters influencing CCL properties.

Table 3: Effective transport parameters determined by GeoDict® for the reconstructed CCL microstructures based on FIB-SEM image data.

	Airbrush	Screen printing	Inkjet	Dry spraying	Doctor blade
Porosity / %	54.83	57.98	60.37	53.01	49.82
D50 / nm	344.3	298.2	352.9	404.9	420.9
Diffusivity / $10^{-6}\, m^2/_s$	4.99	5.42	5.59	4.95	4.39
Permeability / $10^{-15} m^2$	4.61	7.37	8.44	4.67	2.93

To consolidate the results from electrochemical characterization as well as from AFM and FIB-SEM they are summarized in Figure 8. The matrix comprises various properties of the different CCLs showing them as normalized values (Y/Ymax) by the respective maximum among all samples. When discussing this matrix in order to understand which parameters affect MEA performance one needs to keep in mind the polarization curves provided in Figure 1 (A).

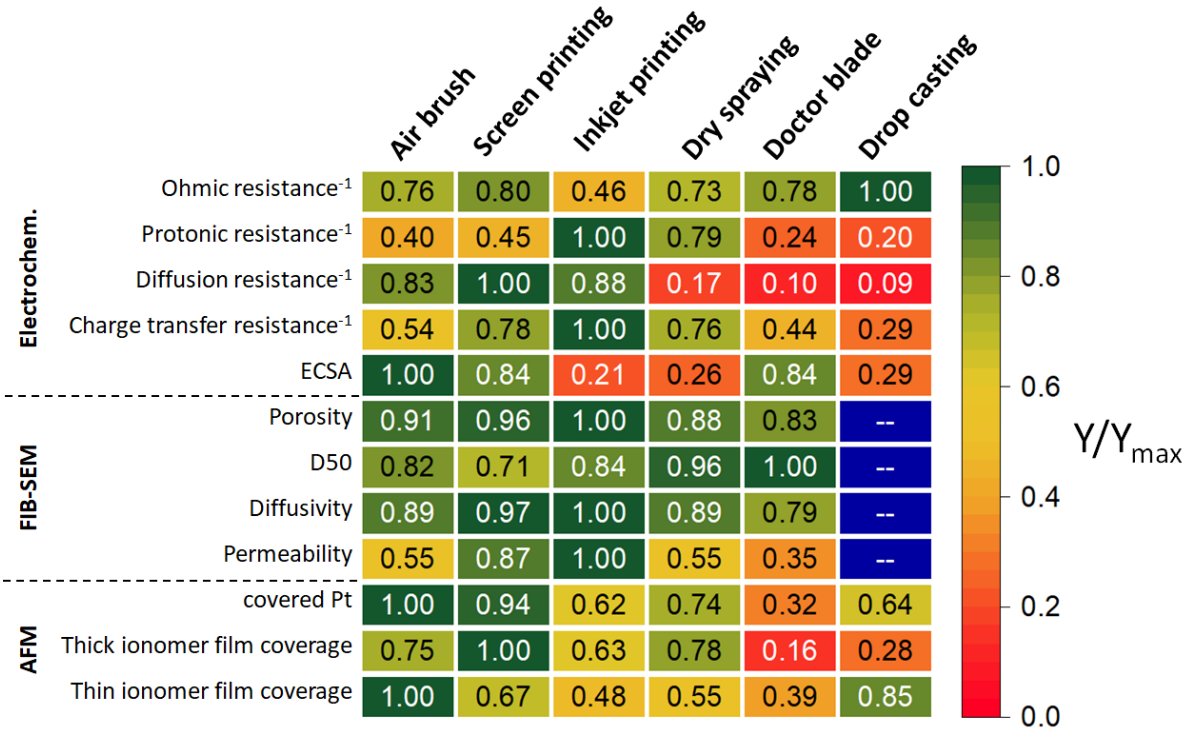

Figure 8: Matrix consolidating results from electrochemical characterization, AFM and FIB-SEM. The columns correspond to individual CCLs. The rows correspond to the evaluated parameters. Within each row the parameters are provided as normalized value (Y/Ymax) related to the maximum values obtained.

The polarization curve of the inkjet printed and drop casted MEAs show low voltages in the kinetic region (~700 mV at 0.05 A cm^{-2}). In case of the inkjet printed MEA, however, one needs to consider that the voltage at 0.05 A cm^{-2} is affected by exceptionally low OCV (870 mV); this

is likely related to a defect in the membrane since the ink jet printed MEA clearly shows highest H_2 cross over among all MEAs prepared using GDEs (see Figure S9 in the Supporting Information). When considering the low OCV in terms of kinetic voltage losses the ink jet printed MEA is comparable with the one preparade using doctor bald. Hence, the highest kinetic losses observed for the drop casted MEA can be reasonably explained by its low ECSA (due to migration of Pt to the GDL, Figure 4 (F)) and high charge transfer resistance. The charge transfer resistance of the inkjet printed MEA is substantially lower.

Great differences in charge transfer resistance as well as in ECSA are apparent when comparing the inkjet printed and the doctor blade MEA; it can be argued that the low ECSA of inkjet CCL (due to formation of Pt agglomerates, Figure 4 (C)) in combination with low charge transfer resistance leads to similar performance as doctor bladed MEA which exhibits high ECSA but also high charge transfer resistance. Noteworthy, the surface of the doctor blade CCL contains large areas of Pt catalyst which is not covered by ionomer which additionally worsens the CCL properties.

Such straightforward explanation is not possible when comparing the performances of inkjet printer MEA with the one prepared using dry spraying (~800 mV at 0.05 A cm^{-2}). Both have similarly low ECSA and rather low charge transfer resistances which is even lower in case of the inkjet printed sample. Opposite properties are linked with the airbrushed MEA which shows the highest cell voltage in the kinetic region of the polarization curve: the ECSA is highest, but the charge transfer resistance is substantially higher as compared to the ink jet printed MEA. Consequently, other parameters than ECSA and charge transfer resistance lead to the clearly higher kinetic losses in the ink jet printed MEA.

At high current densities ohmic and mass transport losses are dominant. It can be seen from the polarization curves in Figure 1 that the slopes of the linear region (e.g. in the range 0.3 - 1.0 Acm^{-2}) do not scale with ohmic resistance. For instance, the slope of the inkjet printed MEA is as low as the one of the screen printed MEA, but the inkjet MEA exhibits significantly higher ohmic resistance (Y/Ymax = 0.46 for inkjet compared to Y/Ymax = 0.80 for screen printing). On the contrary, when plotting the linear slopes of the polarization curves versus diffusion resistance (see Figure S10 in the supporting information) and assuming a linear dependency, a strong correlation (R^2 = 0.935) is observed. Hence, in the conducted experiments diffusion resistance has stronger impact on the polarization curve than ohmic resistance for intermediate current densities. This indicates that transport losses within the catalyst layer contribute significantly to the overall performance loss. The drop casted MEA which has lowest performance also shows lowest protonic conductivity. Additionally, doctor blade and drop casted MEAs both suffer from low gas permeability. Other transport properties such as porosity and diffusivity do not show dramatic differences and therefore their impact on performance cannot be assessed easily. In terms of ionomer distribution, it is noticeable, that MEAs showing poor performance have particularly low fraction of areas with thick ionomer films along with small areas of Pt covered with ionomer hence a quite non-uniform ionomer distribution.

4. Conclusions

Generally, MEAs showing lowest performances (doctor blade and drop casting) exhibit relatively low Y/Ymax values in case of several of the evaluated parameters. On the other hand, MEAs exhibiting relatively high performances (air brush, screen printing and ink jet)

show relatively high Y/Ymax for many of the test properties and do not show very low Y/Ymax for any of the properties. To provide a more detailed assessment it is necessary, however, to discriminate between performances at low and high current densities.

At low current densities the amount of covered Pt/C obtained by AFM seems to be a good measure for the cell performance: Ordering the MEAs with respect to the covered Pt/C we get air brush > screen printing > dry spraying > drop casting > inkjet printing > doctor blade which is quite consistent with the ordering of performance at low current densities except for the doctor blade MEA which performs better than drop casted and inkjet printed MEAs. The increasing performance with increasing covered Pt/C can be explained by the consequent increase in catalyst utilization since Pt covered by ionomer will be accessible to the protons. This also is reflected in the determined ECSA values: CCLs with high fraction of covered Pt/C typically show a higher ECSA (air brush, screen printing) while low fractions of covered Pt/C lead to low ECSA (inkjet printing, dry spraying, drop casting). The doctor blade sample again does not follow this trend as it has a relatively high ECSA despite the observed low fraction of covered Pt/C.

Regarding the performance at high current densities transport properties have to be considered in addition to the catalyst utilization. Porosity, diffusivity and permeability of the different materials obtained by FIB-SEM all show the same trends where inkjet printing has the best transport properties while the lowest values are obtained for the doctor blade sample. Considering the combination of covered Pt/C and the transport properties, the performance ranking at high current densities can be explained. For example, the screen printed sample combines a high fraction of covered Pt/C together with good transport properties, leading to the best performance at high currents. On the other hand, the air brush MEA which has the highest performance at low current densities shows lower performance at

high currents due to the inferior transport properties. The worst performing materials at high current density have low amounts of covered Pt/C in combination with poor transport properties.

5. Acknowledgements

Krishan Talukdar acknowledges financial support by DLR.DAAD research fellowship. Tobias Morawietz and Jan-Fredrik Heger: acknowledge financial support in the frame of FURTHER-FC; FURTHER-FC has received funding from the Fuel Cells and Hydrogen 2 Joint Undertaking under Grant Agreement No 875025. This Joint Undertaking receives support from the European Union's Horizon 2020 Research and Innovation programme, Hydrogen Europe and Hydrogen Europe Research.

6. References

[1] I. Staffell *et al.*, "The role of hydrogen and fuel cells in the global energy system," *Energy & Environmental Science,* 10.1039/C8EE01157E vol. 12, no. 2, pp. 463-491, 2019.

[2] B. C. Steele and A. Heinzel, "Materials for fuel-cell technologies," *Nature,* vol. 414, no. 6861, pp. 345-52, Nov 15 2001.

[3] G. Renouard-Vallet, M. Saballus, G. Schmithals, J. Schirmer, J. Kallo, and K. A. Friedrich, "Improving the environmental impact of civil aircraft by fuel cell technology: concepts and technological progress," *Energy & Environmental Science,* vol. 3, no. 10, p. 1458, 2010.

[4] A. Bauen and D. Hart, "Assessment of the environmental benefits of transport and stationary fuel cells," *Journal of Power Sources,* vol. 86, no. 1-2, pp. 482-494, 3 2000.

[5] S. J. Peighambardoust, S. Rowshanzamir, and M. Amjadi, "Review of the proton exchange membranes for fuel cell applications," *International Journal of Hydrogen Energy,* vol. 35, no. 17, pp. 9349-9384, 9 2010.

[6] D. Papageorgopoulos, "Fuel Cell R&D Overview," presented at the 2019 Annual Merit Review and Peer Evaluation Meeting, 2019. Available: https://www.hydrogen.energy.gov/pdfs/review19/plenary_fuel_cell_papageorgopoulos_2019.pdf

[7] S. T. Thompson and D. Papageorgopoulos, "Platinum group metal-free catalysts boost cost competitiveness of fuel cell vehicles," *Nature Catalysis,* vol. 2, no. 7, pp. 558-561, 2019.

[8] R. Chenitz *et al.*, "A specific demetalation of Fe–N4 catalytic sites in the micropores of NC_Ar + NH3 is at the origin of the initial activity loss of the highly active Fe/N/C catalyst used for the reduction of oxygen in PEM fuel cells," *Energy & Environmental Science,* vol. 11, no. 2, pp. 365-382, 2018.

[9] R. O'Hayre and F. B. Prinz, "The Air/Platinum/Nafion Triple-Phase Boundary: Characteristics, Scaling, and Implications for Fuel Cells," *Journal of The Electrochemical Society,* vol. 151, no. 5, pp. A756 11 K. Karan, Interesting Facets of Surface, Interfacial, and Bulk Characteristics of Perfluorinated Ionomer Films, Langmuir, , DOI:10.1021/acs.langmuir.8b03721., 2004.

[10] K. Karan, "Interesting Facets of Surface, Interfacial, and Bulk Characteristics of Perfluorinated Ionomer Films," *Langmuir,* vol. 35, no. 42, pp. 13489-13520, Oct 22 2019.

[11] H. Liu, W. K. Epting, and S. Litster, "Gas Transport Resistance in Polymer Electrolyte Thin Films on Oxygen Reduction Reaction Catalysts," *Langmuir,* vol. 31, no. 36, pp. 9853-8, Sep 15 2015.

[12] N. L. Garland, D. C. Papageorgopoulos, and J. M. Stanford, "Hydrogen and Fuel Cell Technology: Progress, Challenges, and Future Directions," *Energy Procedia,* vol. 28, pp. 2-11, 2012.

[13] E. A. Ticianelli, C. R. Derouin, A. Redondo, and S. Srinivasan, "Methods to Advance Technology of Proton Exchange Membrane Fuel Cells," *Journal of The Electrochemical Society,* vol. 135, no. 9, pp. 2209-2214, 2019.

[14] J.-H. Wee, K.-Y. Lee, and S. H. Kim, "Fabrication methods for low-Pt-loading electrocatalysts in proton exchange membrane fuel cell systems," *Journal of Power Sources,* vol. 165, no. 2, pp. 667-677, 2007.

[15] Y. Yoon, "Effect of pore structure of catalyst layer in a PEMFC on its performance," *International Journal of Hydrogen Energy,* vol. 28, no. 6, pp. 657-662, 6 2003.

[16] J. Huang, Z. Li, and J. Zhang, "Review of characterization and modeling of polymer electrolyte fuel cell catalyst layer: The blessing and curse of ionomer," *Frontiers in Energy,* vol. 11, no. 3, pp. 334-364, 2017.

[17] K. Malek, T. Mashio, and M. Eikerling, "Microstructure of Catalyst Layers in PEM Fuel Cells Redefined: A Computational Approach," *Electrocatalysis,* vol. 2, no. 2, pp. 141-157, 2011.

[18] G. S. Harzer, A. Orfanidi, H. El-Sayed, P. Madkikar, and H. A. Gasteiger, "Tailoring Catalyst Morphology towards High Performance for Low Pt Loaded PEMFC Cathodes," *Journal of The Electrochemical Society,* vol. 165, no. 10, pp. F770-F779, 2018.

[19] D. R. Baker, D. A. Caulk, K. C. Neyerlin, and M. W. Murphy, "Measurement of Oxygen Transport Resistance in PEM Fuel Cells by Limiting Current Methods," *Journal of The Electrochemical Society,* vol. 156, no. 9, pp. B991 29 K. Talukdar, S. Delgado, T. Lagarteira, P. Gazdzicki and K. A. Friedrich, Minimizing mass-transport loss in proton exchange membrane fuel cell by freeze-drying of cathode catalyst layers, J. Power Sources, 2019, 427, 309–317., 2009.

[20] K. Talukdar, S. Delgado, T. Lagarteira, P. Gazdzicki, and K. A. Friedrich, "Minimizing mass-transport loss in proton exchange membrane fuel cell by freeze-drying of cathode catalyst layers," *Journal of Power Sources,* vol. 427, pp. 309-317, 2019.

[21] M. Ji and Z. Wei, "A Review of Water Management in Polymer Electrolyte Membrane Fuel Cells," *Energies,* vol. 2, no. 4, pp. 1057-1106, 2009.

[22] V. Yarlagadda *et al.*, "Boosting Fuel Cell Performance with Accessible Carbon Mesopores," *ACS Energy Letters,* vol. 3, no. 3, pp. 618-621, 2018.

[23] Z. Yu, R. N. Carter, and J. Zhang, "Measurements of Pore Size Distribution, Porosity, Effective Oxygen Diffusivity, and Tortuosity of PEM Fuel Cell Electrodes," *Fuel Cells,* vol. 12, no. 4, pp. 557-565, 2012.

[24] K. Talukdar, M. A. Ripan, T. Jahnke, P. Gazdzicki, T. Morawietz, and K. A. Friedrich, "Experimental and numerical study on catalyst layer of polymer electrolyte membrane fuel cell prepared with diverse drying methods," *Journal of Power Sources,* vol. 461, 2020.

[25] G. A. Futter, P. Gazdzicki, K. A. Friedrich, A. Latz, and T. Jahnke, "Physical modeling of polymer-electrolyte membrane fuel cells: Understanding water management and impedance spectra," *Journal of Power Sources,* vol. 391, pp. 148-161, 2018.

[26] R. Vetter and J. O. Schumacher, "Free open reference implementation of a two-phase PEM fuel cell model," *Computer Physics Communications,* vol. 234, pp. 223-234, 2019.

[27] B. D. P. Aldebert, G. Gebel, N. Nakamura, M. Pineri, F. Volino "Rod like micellar structures in perfluorinated ionomer solutions," *J. Phys. Chem,* vol. 49, pp. 2101-2109, 1988.

[28] B. Loppinet, G. Gebel, and C. E. Williams, "Small-Angle Scattering Study of Perfluorosulfonated Ionomer Solutions," *The Journal of Physical Chemistry B,* vol. 101, no. 10, pp. 1884-1892, 1997/03/01 1997.

[29] Y. Liu, C. Ji, W. Gu, J. Jorne, and H. A. Gasteiger, "Effects of Catalyst Carbon Support on Proton Conduction and Cathode Performance in PEM Fuel Cells," *Journal of The Electrochemical Society,* vol. 158, no. 6, 2011.

[30] E. Padgett *et al.*, "Mitigation of PEM Fuel Cell Catalyst Degradation with Porous Carbon Supports," *Journal of The Electrochemical Society,* vol. 166, no. 4, pp. F198-F207, 2019.

[31] M. S. Wilson, J. A. Valerio, and S. Gottesfeld, "Low platinum loading electrodes for polymer electrolyte fuel cells fabricated using thermoplastic ionomers," *Electrochimica Acta,* vol. 40, no. 3, pp. 355-363, 1995/02/01/ 1995.

[32] H. Steven, "Fuel Cell Catalyst Layers: A Polymer Science Perspective " *J Chemistry of Materials,* vol. 26, pp. 381-393, 7 2014.

[33] Y.-C. Park, K. Kakinuma, H. Uchida, M. Watanabe, and M. Uchida, "Effects of short-side-chain perfluorosulfonic acid ionomers as binders on the performance of low Pt loading fuel cell cathodes," *Journal of Power Sources,* vol. 275, pp. 384-391, 2015/02/01/ 2015.

[34] Y.-C. Park, H. Tokiwa, K. Kakinuma, M. Watanabe, and M. Uchida, "Effects of carbon supports on Pt distribution, ionomer coverage and cathode performance for polymer electrolyte fuel cells," *Journal of Power Sources,* vol. 315, pp. 179-191, 2016.

[35] A. Kongkanand and M. F. Mathias, "The Priority and Challenge of High-Power Performance of Low-Platinum Proton-Exchange Membrane Fuel Cells," *J Phys Chem Lett,* vol. 7, no. 7, pp. 1127-37, Apr 7 2016.

[36] N. Pramounmat *et al.*, "Controlling the Distribution of Perfluorinated Sulfonic Acid Ionomer with Elastin-like Polypeptide," *ACS Appl Mater Interfaces,* vol. 11, no. 46, pp. 43649-43658, Nov 20 2019.

[37] T. Morawietz, M. Handl, C. Oldani, K. A. Friedrich, and R. Hiesgen, "Quantitative in Situ Analysis of Ionomer Structure in Fuel Cell Catalytic Layers," *ACS Appl Mater Interfaces,* vol. 8, no. 40, pp. 27044-27054, Oct 12 2016.

[38] H. J. Kim, K. Talukdar, Y. H. Kim, Y. Park, H.-C. Lee, and S.-J. Choi, "Study of Semi-Interpenetrating Networks in Nafion®/Polyacrylamide Proton Conducting Membranes," *Journal of Nanoelectronics and Optoelectronics,* vol. 10, no. 4, pp. 569-573, 8 2015.

[39] K. Shinozaki, J. W. Zack, S. Pylypenko, B. S. Pivovar, and S. S. Kocha, "Oxygen Reduction Reaction Measurements on Platinum Electrocatalysts Utilizing Rotating Disk Electrode Technique," *Journal of The Electrochemical Society,* vol. 162, no. 12, pp. F1384-F1396, 2015.

[40] A. Goshtasbi, P. García-Salaberri, J. Chen, K. Talukdar, D. G. Sanchez, and T. Ersal, "Through-the-Membrane Transient Phenomena in PEM Fuel Cells: A Modeling Study," *Journal of The Electrochemical Society,* vol. 166, no. 7, pp. F3154-F3179, 2019.

[41] G. Sasikumar, J. W. Ihm, and H. Ryu, "Dependence of optimum Nafion content in catalyst layer on platinum loading," *Journal of Power Sources,* vol. 132, no. 1-2, pp. 11-17, 2004.

[42] A. Orfanidi, P. Madkikar, H. A. El-Sayed, G. S. Harzer, T. Kratky, and H. A. Gasteiger, "The Key to High Performance Low Pt Loaded Electrodes," *Journal of The Electrochemical Society,* vol. 164, no. 4, pp. F418-F426, 2017.

[43] S. Paul, S.-J. Choi, and H. J. Kim, "Enhanced Proton Conductivity of a Zn(II)-Based MOF/Aquivion Composite Membrane for PEMFC Applications," *Energy & Fuels,* vol. 34, no. 8, pp. 10067-10077, 2020/08/20 2020.

[44] G. Sasikumar, J. W. Ihm, and H. Ryu, "Optimum Nafion content in PEM fuel cell electrodes," *Electrochimica Acta,* vol. 50, no. 2-3, pp. 601-605, 2004.

[45] Y. Liu, C. Ji, W. Gu, D. R. Baker, J. Jorne, and H. A. Gasteiger, "Proton Conduction in PEM Fuel Cell Cathodes: Effects of Electrode Thickness and Ionomer Equivalent Weight," *Journal of The Electrochemical Society,* vol. 157, no. 8, p. B1154, 2010.

[46] Y. Liu *et al.*, "Proton Conduction and Oxygen Reduction Kinetics in PEM Fuel Cell Cathodes: Effects of Ionomer-to-Carbon Ratio and Relative Humidity," *Journal of The Electrochemical Society,* vol. 156, no. 8, p. B970, 2009.

[47] Y. Tabe, M. Nishino, H. Takamatsu, and T. Chikahisa, "Effects of Cathode Catalyst Layer Structure and Properties Dominating Polymer Electrolyte Fuel Cell Performance," *Journal of The Electrochemical Society,* vol. 158, no. 10, 2011.

[48] K. Talukdar *et al.*, "Enveloping of catalyst powder by ionomer for dry spray coating in polymer electrolyte membrane fuel cells," *Journal of Power Sources,* vol. 424, pp. 82-90, 2019.

[49] E. Gülzow *et al.*, "Dry layer preparation and characterisation of polymer electrolyte fuel cell components " *Journal of Power Sources,* vol. 86, pp. 352-362, 3 2000.

[50] M. S. Wilson and S. Gottesfeld, "High Performance Catalyzed Membranes of Ultra-low Pt Loadings for Polymer Electrolyte Fuel Cells," *Journal of The Electrochemical Society,* vol. 139, no. 2, pp. L28-L30, 1992/02/01 1992.

[51] W. M. Mosdale R., Srinivasan S. , "In Fabrication of electrodes for proton exchange membrane fuel cells using a spraying method and their performance evaluation," in *The Electrochemical Society*, Pennington, 1994, p. 179: NJ.

[52] K. Talukdar, P. Gazdzicki, and K. A. Friedrich, "Comparative investigation into the performance and durability of long and short side chain ionomers in Polymer Electrolyte Membrane Fuel Cells," *Journal of Power Sources,* vol. 439, 2019.

[53] F. J. RodrÍguez, P. J. Sebastian, O. Solorza, and R. PÉrez, "Mo–Ru–W chalcogenide electrodes prepared by chemical synthesis and screen printing for fuel cell applications," *International Journal of Hydrogen Energy,* vol. 23, no. 11, pp. 1031-1035, 1998/11/01/ 1998.

[54] C. S. Kim, Y. G. Chun, D. H. Peck, and D. R. Shin, "A novel process to fabricate membrane electrode assemblies for proton exchange membrane fuel cells," *International Journal of Hydrogen Energy,* vol. 23, no. 11, pp. 1045-1048, 1998/11/01/ 1998.

[55] A. Saab, F. Garzon, and T. Zawodzinski, "Determination of Ionic and Electronic Resistivities in Carbon/Polyelectrolyte Fuel-Cell Composite Electrodes," *Journal of The Electrochemical Society,* vol. 149, pp. A1541-A1546, 12/01 2002.

[56] S. Towne, V. Viswanathan, J. Holbery, and P. Rieke, "Fabrication of polymer electrolyte membrane fuel cell MEAs utilizing inkjet print technology," *Journal of Power Sources,* vol. 171, no. 2, pp. 575-584, 2007/09/27/ 2007.

[57] S. Shukla, K. Domican, K. Karan, S. Bhattacharjee, and M. Secanell, "Analysis of Low Platinum Loading Thin Polymer Electrolyte Fuel Cell Electrodes Prepared by Inkjet Printing," *Electrochimica Acta,* vol. 156, pp. 289-300, 2015.

[58] P. Gazdzicki, J. Mitzel, A. M. Dreizler, M. Schulze, and K. A. Friedrich, "Impact of Platinum Loading on Performance and Degradation of Polymer Electrolyte Fuel Cell Electrodes Studied in a Rainbow Stack," (in English), *Fuel Cells,* vol. 18, no. 3, pp. 270-278, Jun 2018.

[59] A. Pozio, M. De Francesco, A. Cemmi, F. Cardellini, and L. Giorgi, "Comparison of high surface Pt/C catalysts by cyclic voltammetry," *Journal of Power Sources,* vol. 105, no. 1, pp. 13-19, 2002/03/05/ 2002.

[60] I. Takahashi and S. S. Kocha, "Examination of the activity and durability of PEMFC catalysts in liquid electrolytes," *Journal of Power Sources,* vol. 195, no. 19, pp. 6312-6322, 2010/10/01/ 2010.

[61] M. B. Sassin, Y. Garsany, B. D. Gould, and K. E. Swider-Lyons, "Fabrication Method for Laboratory-Scale High-Performance Membrane Electrode Assemblies for Fuel Cells," *Anal Chem,* vol. 89, no. 1, pp. 511-518, Jan 3 2017.

[62] S. Shukla, D. Stanier, M. S. Saha, J. Stumper, and M. Secanell, "Analysis of Inkjet Printed PEFC Electrodes with Varying Platinum Loading," *Journal of The Electrochemical Society,* vol. 163, no. 7, pp. F677-F687, 2016.

[63] H. A. Gasteiger, S. S. Kocha, B. Sompalli, and F. T. Wagner, "Activity benchmarks and requirements for Pt, Pt-alloy, and non-Pt oxygen reduction catalysts for PEMFCs," *Applied Catalysis B: Environmental,* vol. 56, no. 1-2, pp. 9-35, 2005.

[64] J. P. Owejan, J. E. Owejan, and W. Gu, "Impact of Platinum Loading and Catalyst Layer Structure on PEMFC Performance," *Journal of The Electrochemical Society,* vol. 160, no. 8, pp. F824-F833, 2013.

[65] M. B. Sassin, Y. Garsany, B. D. Gould, and K. Swider-Lyons, "Impact of Compressive Stress on MEA Pore Structure and Its Consequence on PEMFC Performance," *Journal of The Electrochemical Society,* vol. 163, no. 8, pp. F808-F815, 2016.

[66] C. Simon, F. Hasché, and H. A. Gasteiger, "Influence of the Gas Diffusion Layer Compression on the Oxygen Transport in PEM Fuel Cells at High Water Saturation Levels," *Journal of The Electrochemical Society,* vol. 164, no. 6, pp. F591-F599, 2017.

[67] M. C. Lefebvre, "Characterization of Ionic Conductivity Profiles within Proton Exchange Membrane Fuel Cell Gas Diffusion Electrodes by Impedance Spectroscopy," *Electrochemical and Solid-State Letters,* vol. 2, no. 6, 1999.

[68] G. Li and P. G. Pickup, "Ionic Conductivity of PEMFC Electrodes," *Journal of The Electrochemical Society,* vol. 150, no. 11, 2003.

[69] P. C. Fortunato Migliardini, "CV and EIS Study of Hydrogen Fuel Cell Durability in Automotive Applications," *Int. J. Electrochem. Sci.,* vol. 8, pp. 11033-11047, 2013.

[70] S. Shukla, K. Domican, and M. Secanell, "Analysis of Kinetic Parameters and Effect of Pt Loading on Cell Performance of PEFC Electrodes Prepared by Inkjet Printing," *ECS Transactions,* vol. 69, no. 17, pp. 761-772, 10 2015.

[71] P. Boillat, L. Gubler, F. N. Büchi, and T. J. Schmidt, "Use and misuse of electrochemical impedance spectroscopy in PEFC research," presented at the 236th ECS Meeting, Atlanta GA, USA, 2019.

[72] M. Eikerling and A. A. Kornyshev, "Electrochemical impedance of the cathode catalyst layer in polymer electrolyte fuel cells," *J. Electroanal. Chem.,* vol. 475, pp. 107-123, 10 1999.

[73] J. Schindelin *et al.*, "Fiji: an open-source platform for biological-image analysis," *Nat Methods,* vol. 9, no. 7, pp. 676-82, Jun 28 2012.

[74] (2020). *Geodict*. Available: https://www.math2market.com/

[75] N. Otsu, "A Threshold Selection Method from Gray-Level Histograms," *IEEE Transactions on Systems, Man, and Cybernetics,* vol. 9, no. 1, pp. 62-66, 1 1979.

[76] C. S. Kong, D. Y. Kim, H. K. Lee, Y. G. Shul, and T. H. Lee, "Influence of pore-size distribution of diffusion layer on mass-transport problems of proton exchange membrane fuel cells," (in English), *Journal of Power Sources,* vol. 108, no. 1-2, pp. 185-191, Jun 1 2002.

[77] N. Zamel, "The catalyst layer and its dimensionality - A look into its ingredients and how to characterize their effects," (in English), *Journal of Power Sources,* vol. 309, pp. 141-159, Mar 31 2016.

[78] M. Eikerling, "Water management in cathode catalyst layers of PEM fuel cells - A structure-based model," (in English), *Journal of the Electrochemical Society,* vol. 153, no. 3, pp. E58-E70, 2006.

[79] W. G. Pollard and R. D. Present, "On Gaseous Self-Diffusion in Long Capillary Tubes," *Physical Review,* vol. 73, no. 7, pp. 762-774, 04/01/ 1948.